ADVANCED MATERIALS

www.advmat.de

Extremely Vivid, Highly Transparent, and Ultrathin Quantum Dot Light-Emitting Diodes

Moon Kee Choi, Jiwoong Yang, Dong Chan Kim, Zhaohe Dai, Junhee Kim, Hyojin Seung, Vinayak S. Kale, Sae Jin Sung, Chong Rae Park, Nanshu Lu, Taeghwan Hyeon, and Dae-Hyeong Kim**

Displaying information on transparent screens offers new opportunities in next-generation electronics, such as augmented reality devices, smart surgical glasses, and smart windows. Outstanding luminance and transparency are essential for such "see-through" displays to show vivid images over clear background view. Here transparent quantum dot light-emitting diodes (Tr-QLEDs) are reported with high brightness (bottom: ≈43 000 cd m^{-2}, top: ≈30 000 cd m^{-2}, total: ≈73 000 cd m^{-2} at 9 V), excellent transmittance (90% at 550 nm, 84% over visible range), and an ultrathin form factor (≈2.7 µm thickness). These superb characteristics are accomplished by novel electron transport layers (ETLs) and engineered quantum dots (QDs). The ETLs, ZnO nanoparticle assemblies with ultrathin alumina overlayers, dramatically enhance durability of active layers, and balance electron/hole injection into QDs, which prevents nonradiative recombination processes. In addition, the QD structure is further optimized to fully exploit the device architecture. The ultrathin nature of Tr-QLEDs allows their conformal integration on various shaped objects. Finally, the high resolution patterning of red, green, and blue Tr-QLEDs (513 pixels $in.^{-1}$) shows the potential of the full-color transparent display.

Dr. M. K. Choi, Dr. J. Yang, D. C. Kim, J. Kim, H. Seung, V. S. Kale, Prof. T. Hyeon, Prof. D.-H. Kim
Center for Nanoparticle Research
Institute for Basic Science (IBS)
Seoul 08826, Republic of Korea
E-mail: thyeon@snu.ac.kr; dkim98@snu.ac.kr

Dr. M. K. Choi, Dr. J. Yang, D. C. Kim, J. Kim, H. Seung, V. S. Kale, Prof. T. Hyeon, Prof. D.-H. Kim
School of Chemical and Biological Engineering
Institute of Chemical Processes
Seoul National University
Seoul 08826, Republic of Korea

Z. Dai, Prof. N. Lu
Center for Mechanics of Solids
Structures and Materials
Department of Aerospace Engineering and Engineering Mechanics
Department of Biomedical Engineering
Texas Materials Institute
University of Texas at Austin
Austin, TX 78712, USA

S. J. Sung, Prof. C. R. Park
Research Institute of Advanced Materials
Department of Materials Science and Engineering
Seoul National University
Seoul 08826, Republic of Korea

DOI: 10.1002/adma.201703279

Transparent displays lie at the heart of next generation optoelectronics[1,2] in the era of augmented reality (AR), wearable electronics, and internet of things (IoTs).[3–7] Being transparent for light-emitting diodes (LEDs) significantly expands their applications by displaying visual information on objects without affecting their original appearance and functionality. However, there has been a large gap in the electroluminescence (EL) performance between transparent displays and non-transparent counterparts,[8] due in large part to imbalanced injection of charge carriers into the emitter, unoptimized energy band alignment of the top electrode, and vulnerability of organic and/or polymeric light emitting materials during the deposition of transparent conducting oxide electrodes.[9–12] The previous progresses and unmet requirements for transparent displays are described in Section S2.1, Figure S1, and Table S1 of the Supporting Information. In addition, there has been much need to develop novel device architectures[13–16] that consider the carrier dynamics for high-performance transparent quantum dot light-emitting diodes (Tr-QLEDs).

For high-quality transparent displays, first of all, high transparency is an absolute requirement.[17] The effect of transparency on visibility of background is examined on the university logo and a leaf (**Figure 1**a). For transparency below 70% (semitransparency), the color and contrast of objects behind the display are significantly deteriorated. In contrast, Tr-QLEDs of 84% transparency present clear background view in both cases. Secondly, high brightness and color purity are particularly important for vividness of "see-through" displays. The maximum brightness of conventional displays (e.g., smart phones and monitors) is around 600 cd m^{-2}. For see-through displays, however, the displayed information becomes blurred at this brightness (i.e., 600 cd m^{-2}) because of photointerference with ambient light (Figure 1b; Figure S2a, Supporting Information). Therefore, significantly higher brightness is required to ensure clear and vivid displays (Figure 1b). In addition, chromatic aberrations can be minimized by employing engineered quantum dots (QD) emitters[18,19] that exhibit better color purity than organic and/or polymer emitters (Figure S2b, Supporting Information). Lastly, integration of highly deformable

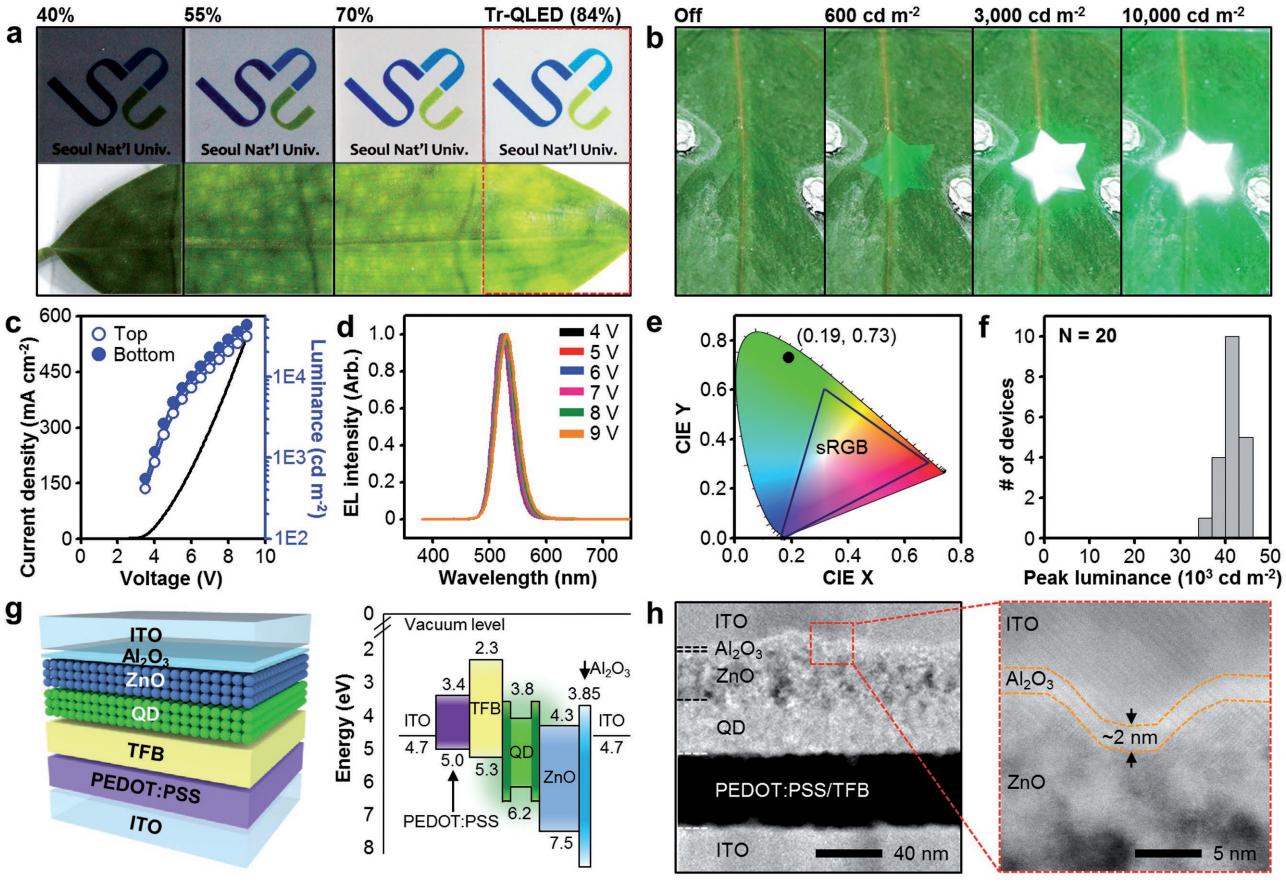

Figure 1. Extremely vivid, highly transparent quantum dot light emitting diode. a) Effect of transparency on visibility of background: the university logo (top) and a leaf (bottom). b) Effect of brightness on vividness of the display under ambient light. c) *J*–*V*–*L* characteristics, d) EL spectra, and e) CIE 1931 *x*–*y* chromaticity diagram of Tr-QLEDs. f) Histogram of peak luminance of Tr-QLEDs ($N = 20$). g) Schematic illustration of the device structure (left) and energy-band diagram (right) of the Tr-QLED. The band edges are estimated by ultraviolet photoelectron spectroscopy. h) Cross-sectional scanning TEM image of the Tr-QLED (left) and magnified view of the ETL_{A_2} (right).

transparent displays on various curved objects (Figure S2c, Supporting Information) is desirable in smart wearables and AR/IoT devices.[20–24] Highly transparent and deformable displays not only improve aesthetic factors of the system design but also enable stacking of optical information.

Our Tr-QLEDs show the highest brightness (bottom emission: ≈43 000 cd m^{-2}, top emission: ≈30 000 cd m^{-2}, and total emission: ≈73 000 cd m^{-2} at 9 V) and transmittance (90% at 550 nm, 84% over visible range) among transparent LEDs reported to date (Figure 1c; Figure S1 and Table S1, Supporting Information). The Tr-QLEDs show pure green emission (Figure 1d) corresponding to the Commission Internationale de l'Eclairage coordinates (0.19, 0.73; Figure 1e), and good reproducibility of the peak luminance (Figure 1f). Unless otherwise stated, the EL characteristics of Tr-QLEDs below are based on bottom emission. Unique materials and device design strategies made it possible to achieve these excellent characteristics. The advanced device architecture for the Tr-QLED and the energy band diagram of materials are described in Figure 1g. All components are carefully selected by considering the energy level, carrier mobility, and solvent orthogonality. The layer structures are characterized by cross-sectional transmission electron microscopy (TEM; Figure 1h): hole transporting layers (HTLs; poly(3,4-ethylenedioxythiophene):poly(styrene sulfonate) (PEDOT:PSS) and poly[(9,9-dioctylfluorenyl-2,7-diyl)-*co*-(4,4′-(*N*-(4-sec-butylphenyl)diphenylamine))] (TFB); 20 nm each), colloidal QD emitters (40 nm), and electron transport layers (ETLs) (ZnO nanoparticles (33 nm) with alumina overlayer (2 nm)) between the indium tin oxide (ITO) anode and cathode (100 nm each). The detailed fabrication process is described in the Supporting Information.

The remarkable EL performance and transparency are attributed to the newly designed ETL (ETL_{A_x}: defined as ZnO nanoparticle assemblies with alumina overlayers of x nm thickness), which enables application of the top ITO electrode without sacrificing the device performance and balances electron/hole injection into QD emitters. The alumina overlayer is formed by oxidation of a thermally evaporated ultrathin Al layer on the ZnO nanoparticle assembly. Scanning TEM (annular bright field mode and energy dispersive X-ray spectroscopy mode) and X-ray photoelectron spectroscopy analysis confirm successful formation of the conformally overlaid alumina layers (Figure S3, Supplementary Information). The use of ITO as a top electrode leads to outstanding transparency of 84% in the

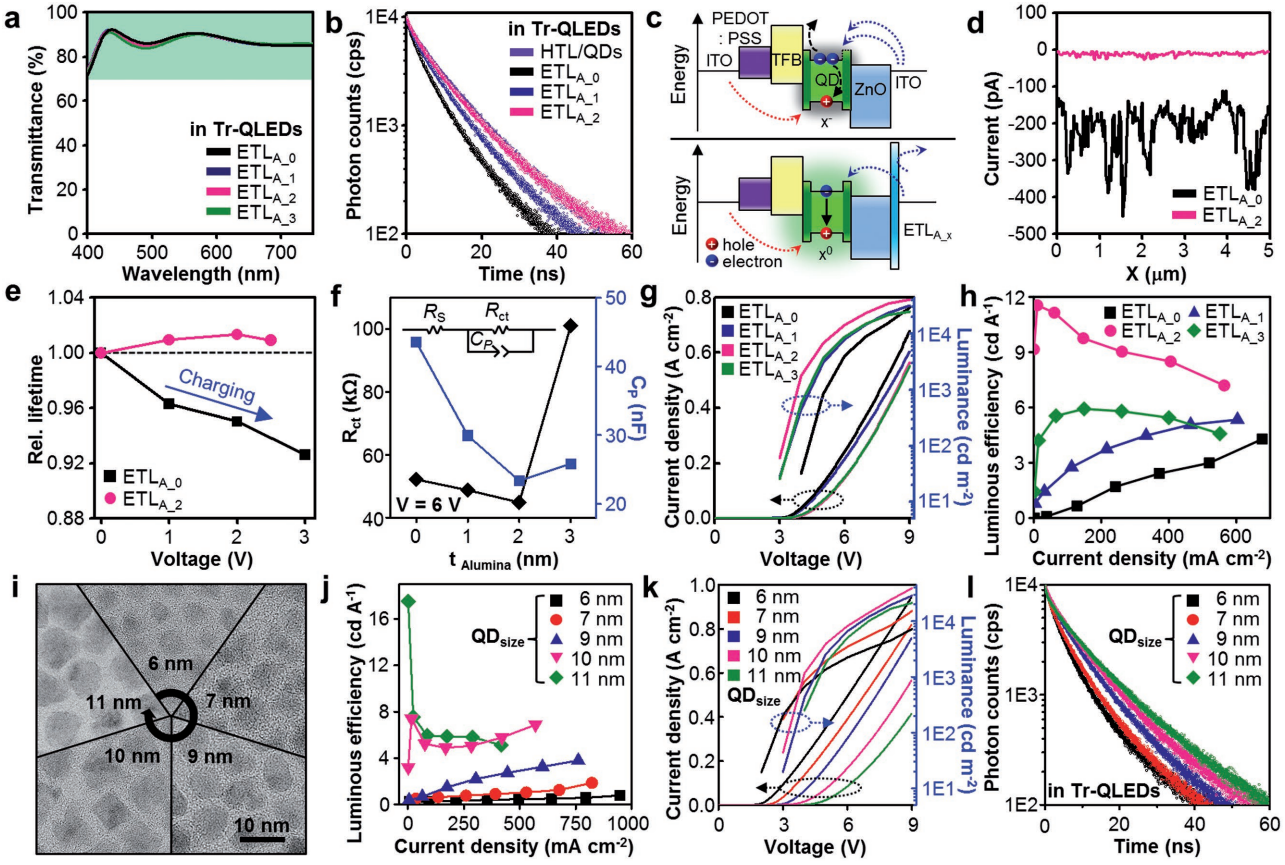

Figure 2. Optimization and characterization of ETLs and QDs for Tr-QLEDs. a) Transmittance spectra of Tr-QLEDs with the ETL_{A_x}. b) Time-resolved PL spectra of QDs in Tr-QLEDs with respect to the ETL_{A_x}. c) Schematic illustration showing the balanced carrier injection in Tr-QLEDs with the ETL_{A_x}. d) Current distribution of the ETL_{A_x} characterized by conductive AFM. e) Exciton carrier lifetime of QDs in Tr-QLEDs with ETL_{A_0} and ETL_{A_2} as a function of the applied voltage. f) Charge transport resistance (R_{ct}; left axis) and capacitance (C_P; right axis) of the Tr-QLEDs at 6 V with respect to the alumina thickness. Inset shows the equivalent circuit model. g) *J–V–L* characteristics and h) luminous efficiency of Tr-QLEDs with respect to the ETL_{A_x}. i) TEM images of core–shell QDs with different shell thicknesses. j) Luminous efficiency and k) *J–V–L* characteristics of the Tr-QLEDs employing QDs with different shell thicknesses. l) Time-resolved PL spectra of core–shell QDs with different shell thicknesses in Tr-QLEDs.

visible range (400–700 nm) and 90% at 550 nm (**Figure 2**a). The change in transmittance as stacking the composing layers of the Tr-QLED is shown in Figure S4 (Supporting Information). By using the highly transparent top ITO electrode (>90%) and the ultrathin alumina overlayer of ETL_{A_2} (≈99%), the improved device performance was achieved while maintaining the high transmittance.

To investigate the protective role of the ETL_{A_x} during the top electrode deposition, we exposed the ETL_{A_x}-coated QD films to Ar plasma (30 W, 13 Pa). The photoluminescence (PL) intensity of QDs with the ETL_{A_2} (ZnO nanoparticle assemblies with the 2 nm alumina overlayer) is preserved under the plasma treatment, while that of QDs with the ETL_{A_0} (ZnO nanoparticle assemblies) is significantly decreased (Figure S5a, Supporting Information). Time-resolved PL (TRPL) analysis of QDs within the full device also supports this protective effect of the ETL_{A_2} (Figure 2b). The carrier lifetime of QDs without the overlayer is smaller than that of QDs with ETL_{A_2} (Figure S5b, Supporting Information) because of the nonradiative defect-induced transition caused by mechanical damages. Additionally, a simple diode test also supports the protective role of ETL_{A_x} (Figure S6, Supporting Information). The device lifetime of Tr-QLEDs is measured to verify the effect of ETL modification. Without ETL modification (ETL_{A_0}), more than half of fabricated devices are short-circuited and show poor device performance due to physical and/or chemical damages during the top electrode deposition procedure. As a result, the device lifetime with ETL_{A_0} is very short, less than 1 h at 1500 cd m^{-2}, and the device lifetime variation between devices is large. On the other hand, as shown in Figure S7 of the Supporting Information, the lifetime of the Tr-QLED with ETL_{A_2} is about 23.8 h at 3.4 mA applied current (I_0 = 1509 cd m^{-2}), which corresponds to the device lifetime of 1395 h at 100 cd m^{-2} (lifetime × $I_0^{1.5}$ = const.). This value is at least 2 orders higher than the Tr-QLEDs with ETL_{A_0}, which indicates that ETL_{A_2} can prevent the plasma damage and enhance the device performance.

In addition to the protection role, the ETL_{A_x} balances electron/hole injection into QDs, which is critical for efficient radiative recombination.[25–27] Figure 2c illustrates the suggested charge transport mechanism with the ETL_{A_x}. The exciton states of QDs are easily charged by excess electrons because the electron mobility of the ZnO nanoparticle assembly is one

order of magnitude higher than the hole mobility of TFB. This induces nonradiative recombination pathways associated with the Auger process,[28,29] causing efficiency roll-off (Figure 2c, top). The ETL_{A_x}, however, prevents excessive electron injection coming from the cathode (Figure 2c, bottom). This does not affect the electron transfer between QDs and ZnO nanoparticles, since the alumina overlayer is located between ZnO nanoparticles and the cathode. Furthermore, the ETL_{A_x} significantly enhances areal homogeneity of the current distribution (Figure 2d) without affecting the surface topology (Figure S8, Supporting Information). In conductive atomic force microscopy (AFM) analysis, several spikes of the current are observed in the ETL_{A_0}, which can cause short-circuiting within the device, while the ETL_{A_2} exhibits uniform current distribution without such current spikes (Figure S9, Supporting Information).

To examine the effect of the ETL_{A_x} on the carrier dynamics, the TRPL spectra of QDs in Tr-QLEDs were measured under applied biases (Figure S10, Supporting Information).[30] Without the alumina overlayers, the QD carrier lifetime progressively decreases under the applied bias because of the increasing contribution of charged states (Figure 2e). In contrast, PL decay with the ETL_{A_2} is unaffected by the applied bias, suggesting that the modified ETL preserves charge neutrality of QDs during the device operation. This highlights that balanced hole/electron injection and controlled carrier recombination are more important than simply enhancing the carrier injection rate. In addition, electrochemical impedance analysis reveals that the ETL_{A_x} not only balances injection of electrons/holes but also enhances the charge kinetics of the device despite using insulating overlayers (Figure 2f; Figure S11, Supporting Information). The charge transport resistance (R_{ct}) and capacitance (C_p) are obtained by the equivalent circuit model (Figure 2f, inset). Tr-QLEDs with the overlayers (except the thickest one) show the low R_{ct} and C_p, particularly with the ETL_{A_2} (Figure 2f; at 6 V). The changes in C_p and R_{ct} depending on the applied voltage (Figure S11c,d, Supporting Information) imply that the overlayer with optimized thickness effectively suppresses device charging and enhances the charge transport. See Section S2.2 and Figure S11 in the Supporting Information for more detailed explanation and data.

The EL performance is dramatically improved by the ETL_{A_2} (Figure 2g,h). The luminance and efficiency of Tr-QLEDs are enhanced by optimizing the overlayer thickness, while the turn-on voltage of the Tr-QLEDs remains similar (Figure 2g,h). Note that Tr-QLEDs with the optimized ETL (i.e., ETL_{A_2}) present remarkable luminance (≈43 000 cd m^{-2} at 9 V; bottom emission) and low turn-on voltage (≈3 V) without luminance roll-off, which is attributed to the protection of active layers and balanced charge-injection into QDs. Tr-QLEDs with ETL_{A_3} show decreased luminance and luminance efficiency, because the thick alumina overlayer acts as an insulation layer and restricts electron transfer from the cathode. Conventionally, plasma enhanced atomic layer deposition (PEALD) has been used to fabricate ultrathin metal oxide layer. However, introduction of PEALD-based alumina overlayer decreases the device performance of Tr-QLEDs, because the plasma-based atomic layer deposition procedure causes damages to the QD emitters (Figure S12, Supporting Information). Therefore, we introduce the ultrathin alumina overlayer through oxidation of thermally evaporated aluminum.

Another effort to improve the EL performance is structural engineering of QDs.[31–36] We prepared a series of alloyed core/shell CdSe/ZnS QDs by growing ZnS shells of different thicknesses, which show high color purity (full width at half maximum (FWHM) of ≈30 nm) and PL quantum yield (>80%) (see Figure S13 and Section Methods of the Supporting Information for detailed synthetic procedures). The QD size is measured by TEM images (6, 7, 9, 10, and 11 nm; Figure 2i; Figure S13a, Supporting Information) and confirmed by elemental mapping images (Figure S13b, Supporting Information). In contrast to general cases, the QD bandgaps slightly increase as the shell thickness increases (Figure S13d, Supporting Information). This implies formation of alloyed core–shell interfaces by atomic interdiffusion during high-temperature shell growth, which is beneficial for effective carrier injection into QDs.[37]

The QD structure engineering significantly enhances stability of QD films (Figure S13e, Section S2.3, Supporting Information) and performance of Tr-QLEDs (Figure 2j). As the shell thickness increases, the Tr-QLEDs show reduced current density and high turn-on voltage because the thick shell acts as a charge injection barrier (Figure 2k). Meanwhile, nonradiative recombination of QDs in Tr-QLEDs (e.g., Auger recombination) is suppressed as the shell thickness increases as shown in TRPL data (Figure 2l; Figure S13f, Supporting Information). With this compensation, brightness is maximized with 10 nm QDs and total external quantum efficiency (EQE) reaches to 10% (bottom: ≈6%, top: ≈4%) with 11 nm QDs. For the optimization, we also varied the thickness of QD layer (Figure S14a, Supporting Information). As the QD thickness decreases from 45 to 34 nm, Tr-QLEDs show lower turn-on voltage and higher luminance. In addition, ligands of QDs are also optimized for the high performance Tr-QLEDs (Figure S14b, Section S2.4, Supporting Information). Based on these optimizations, we employed oleic acid-capped 10 nm QDs for Tr-QLEDs because of their high brightness.

The ultrathin form factor of Tr-QLEDs (2.7 μm total thickness; **Figure 3**a) allows high deformability,[38,39] which enables transparent displays on various curved objects.[40,41] The 330 nm thick Tr-QLED is designed to be located near the neutral mechanical plane between 1.2 μm thick parylene/epoxy double-layered encapsulation (Figure S15, Supporting Information). This design effectively minimizes the induced strain under mechanical deformations (e.g., bending, folding, and wrinkling) without any efficiency roll-off (Figure 3b–e; Movie S1, Supporting Information). Moreover, the 1.2 μm thick double-layered encapsulation shows low water vapor permeability (0.07 g mm m^{-2} d^{-1}) and oxygen permeability (0.6 cc mm m^{-2} d^{-1}), which indicates effective protection of the ultrathin Tr-QLEDs from potential water/oxygen damages. The performance of ultrathin Tr-QLEDs is highly stable regardless of the bending radius (Figure 3c) and after 1000 bending cycles (Figure 3d). Introducing the wavy structure (buckles of ≈360 μm wavelength and ≈100 μm amplitude; Figure S16a–c, Supporting Information) provides mechanical advantages, leading to an effective level of stretchability (Figure 3e). As shown in Figure S16d of the Supporting Information, the radius of curvature of the wavy structure in Tr-QLEDs (0% strain) ranges from a few micrometers to hundreds of micrometers. The peak strain in stretchable Tr-QLEDs

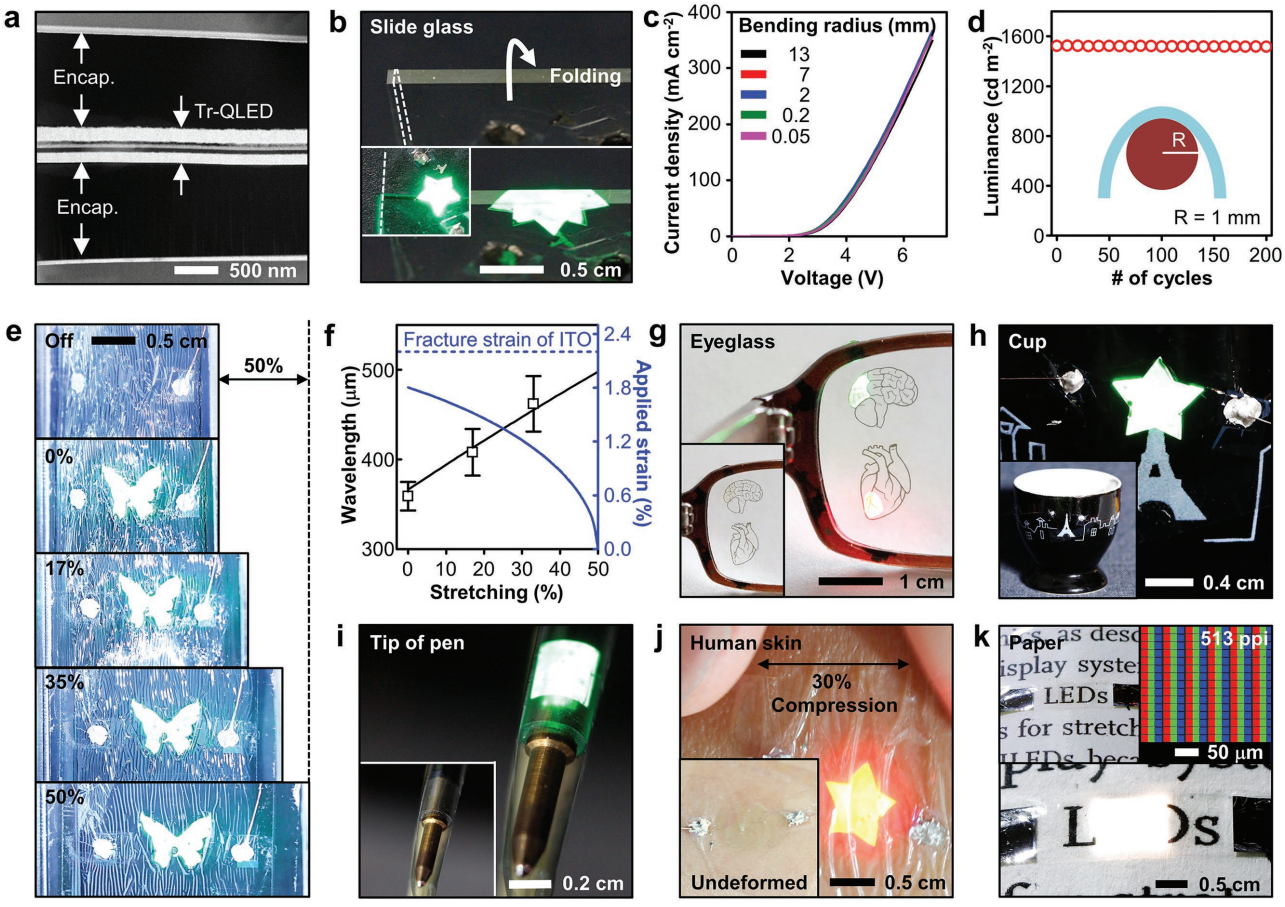

Figure 3. Ultrathin Tr-QLEDs and deformable characteristics. a) Cross-sectional TEM image of the ultrathin Tr-QLED. b) Ultrathin Tr-QLEDs folded on the edge of a slide glass. c) *J*–*V* characteristics at various bending radii. d) Durability test of the ultrathin Tr-QLED. Inset shows the bending radius (R = 1 mm). e) Ultrathin deformable Tr-QLEDs which is sequentially stretched up to 50% without any luminance changes. f) Changes in the wavelength and maximum strain of Tr-QLEDs with the applied tensile strain. g–i) Ultrathin Tr-QLEDs laminated on various curved substrates; Tr-QLEDs on eyeglasses (g), a cup (h), and the tip of a pen (i). Inset of each figure shows the off-state of Tr-QLEDs. j) Deformed Tr-QLEDs (30% compression) on human skin. Inset shows the off-state of undeformed Tr-QLEDs. k) White Tr-QLEDs based on a RGB Tr-QLED array. The array is patterned by the intaglio transfer printing method (513 pixels in^{-1}) and laminated on the paper. Inset shows the off-state of white Tr-QLEDs (left) and magnified PL image of RGB pixels (right).

is predicted to be less than the fracture strain of ITO (≈2.2%) through analytical modeling (Section S2.5, Supporting Information). When the stretchable Tr-QLED is subjected to tension, the peak strain in the device decreases with the applied tensile strain as it is a wrinkle-releasing process (Figure 3f). Consequently, the device can be deformed without any luminance decrease even after stretching up to 50% (Figure 3e).

With this outstanding deformability, Tr-QLEDs can be seamlessly integrated on objects of various curvatures (e.g., eyeglasses, a ball, a tip of a pen, a car window, a glass, and a cup; Figure 3g–i; Figure S17, Supporting Information) without affecting the original appearance or functionality of the object. For instance, Figure 3g shows bicolored Tr-QLEDs mounted on eyeglasses; such eyeglasses with integrated Tr-QLEDs can support surgeons by displaying the patient's medical information overlaid on the surgical site (e.g., vital signs, X-ray images, and computed tomography (CT)/magnetic resonance imaging (MRI) scans) and increase surgical efficiency during operations. The ultrathin Tr-QLED can be conformally integrated even on the human skin, which is an extreme case of the soft, curved, and deformable surface (Figure 3j). In addition, Tr-QLEDs with precisely aligned red, green, and blue (RGB) pixels with a resolution of 513 pixels $in.^{-1}$ are successfully fabricated using the transfer-printing technique (Figure 3k).[38,42,43] The high resolution pattering of ultrathin RGB Tr-QLEDs exhibits the potential for the deformable full-color transparent display.[44,45]

This work presents highly bright and transparent QD-LEDs with an ultrathin form factor and high color purity. The Tr-QLED performance is dramatically enhanced by engineering the ETL and QD structure. The ETL, which consists of a thin alumina layer over the ZnO nanoparticle assembly, provides protection to active layers and balances carrier injection into QDs. These device and material innovations lead to superior luminance (bottom: ≈43 000 cd m^{-2}, top: ≈30 000 cd m^{-2}, total: ≈73 000 cd m^{-2} at 9 V) and extreme transparency (90% at 550 nm, 84% over the visible range). Ultrathin nature of the transparent display (thickness: 2.7 μm) allows its conformal integration on various curved objects. The devices also maintain

the stable performance under a wide range of deformation modes (bending, folding, and stretching). This Tr-QLED technology would expedite the development of next-generation electronics including AR, IoT, and wearable devices.

Experimental Section

A detailed description of procedures and characterization methods are available in the Supporting Information. To conduct the experiment using skin-attachable devices on human skin, informed consent from the subjects to participate in the experiment was obtained and no permission was required from the institute.

Supporting Information

Supporting Information is available from the Wiley Online Library or from the author.

Acknowledgements

M.K.C., J.Y. and D.C.K. contributed equally to this work. This research was supported by IBS-R006-D1 and IBS-R006-A1. This work was also supported by a Seoul National University Research Grant.

Conflict of Interest

The authors declare no conflict of interest.

Keywords

light-emitting diodes, quantum dots, transparent displays, ultrathin electronics, wearable electronics

Received: June 12, 2017
Revised: September 2, 2017
Published online:

[1] C. W. Hsu, B. Zhen, W. Qiu, O. Shapira, B. G. DeLacy, J. D. Joannopoulos, M. Soljačić, *Nat. Commun.* **2014**, *5*, 3152.
[2] P. Jing, W. Ji, Q. Zeng, D. Li, S. Qu, J. Wang, D. Zhang, *Sci. Rep.* **2015**, *5*, 12499.
[3] H. Kim, E. Brueckner, J. Song, Y. Li, S. Kim, C. Lu, J. Sulkin, K. Choquette, Y. Huang, R. G. Nuzzo, J. A. Rogers, *Proc. Natl. Acad. Sci. USA* **2011**, *108*, 10072.
[4] E. Downing, L. Hesselink, J. Ralston, R. Macfarlane, *Science* **1996**, *273*, 1185.
[5] C. Wang, D. Hwang, Z. Yu, K. Takei, J. Park, T. Chen, B. Ma, A. Javey, *Nat. Mater.* **2013**, *12*, 899.
[6] X. Dai, Y. Deng, X. Peng, Y. Jin, *Adv. Mater.* **2017**, *29*, 1607022.
[7] M. K. Choi, I. Park, D. C. Kim, E. Joh, O. K. Park, J. Kim, M. Kim, C. Choi, J. Yang, K. W. Cho, J.-H. Hwang, J.-M. Nam, T. Hyeon, J. H. Kim, D.-H. Kim, *Adv. Funct. Mater.* **2015**, *25*, 7109.
[8] H. Y. Kim, Y. J. Park, J. Kim, C. J. Han, J. Lee, Y. Kim, T. Greco, C. Ippen, A. Wedel, B.-K. Ju, M. S. Oh, *Adv. Funct. Mater.* **2016**, *26*, 3454.
[9] W. Wang, H. Peng, S. Chen, *J. Mater. Chem. C* **2016**, *4*, 1838.
[10] J. Meyer, T. Winkler, S. Hamwi, S. Schmale, H.-H. Johannes, T. Weimann, P. Hinze, Q. Kowalsky, T. Riedl, *Adv. Mater.* **2008**, *20*, 3839.
[11] J. Liang, L. Li, X. Niu, Z. Yu, Q. Pei, *Nat. Photonics* **2013**, *7*, 817.
[12] V. Wood, M. J. Panser, J.-M. Caruge, J. E. Halpert, M. G. Bawendi, V. Bulović, *Nano Lett.* **2010**, *10*, 24.
[13] T. Zhao, E. D. Goodwin, J. Guo, H. Wang, B. T. Diroll, C. B. Murray, C. R. Kagan, *ACS Nano* **2016**, *10*, 9267.
[14] C. R. Kagan, E. Lifshitz, E. H. Sargent, D. V. Talapin, *Science* **2016**, *353*, aac5523.
[15] Z.-K. Tan, R. S. Moghaddam, M. L. Lai, P. Docampo, R. Higler, F. Deschler, M. Price, A. Sadhanala, L. M. Pazos, D. Credgington, F. Hanusch, T. Bein, H. J. Snaith, R. H. Friend, *Nat. Nanotechnol.* **2015**, *9*, 687.
[16] J.-Y. Kim, J. Yang, J. H. Yu, W. Baek, C.-H. Lee, H. J. Son, T. Hyeon, M. J. Ko, *ACS Nano* **2015**, *9*, 11286
[17] J.-K. Song, D. Son, J. Kim, Y. J. Yoo, G. J. Lee, L. Wang, M. K. Choi, J. Yang, M. Lee, K. Do, J. H. Koo, N. Lu, J. H. Kim, T. Hyeon, Y. M. Song, D.-H. Kim, *Adv. Funct. Mater.* **2017**, *27*, 1605286.
[18] V. L. Colvin, M. C. Schlamp, A. P. Alivisatos, *Nature* **1994**, *370*, 354.
[19] Y. Shirasaki, G. J. Supran, M. G. Bawendi, V. Bulović, *Nat. Photonics* **2013**, *7*, 13.
[20] T. Yokota, P. Zalar, M. Kaltenbrunner, H. Jinno, N. Matsuhisa, H. Kitanosako, Y. Tachibana, W. Yukita, M. Koizumi, T. Someya, *Sci. Adv.* **2016**, *2*, e1501856.
[21] M. S. White, M. Kaltenbrunner, E. D. Głowacki, K. Gutnichenko, G. Kettlgruber, I. Graz, S. Aazou, C. Ulbricht, D. A. M. Egbe, M. C. Miron, Z. Major, M. C. Scharber, T. Sekitani, T. Someya, S. Bauer, N. S. Sariciftci, *Nat. Photonics* **2013**, *7*, 811.
[22] T. Sekitani, H. Nakajima, H. Maeda, T. Fukushima, T. Aida, K. Hata, T. Someya, *Nat. Mater.* **2009**, *8*, 494.
[23] Y. Wang, C. Zhu, R. Pfattner, H. Yan, L. Jin, S. Chen, F. Molina-Lopez, F. Lissel, J. Liu, N. I. Rabiah, Z. Chen, J. W. Chung, C. Linder, M. F. toney, B. Murmann, Z. Bao, *Sci. Adv.* **2017**, *3*, e1602076.
[24] D. Son, S. I. Chae, M. Kim, M. K. Choi, J. Yang, K. Park, V. S. Kale, J. H. Koo, C. Choi, M. Lee, J. H. Kim, T. Hyeon, D.-H. Kim, *Adv. Mater.* **2016**, *28*, 9326.
[25] B. S. Mashford, M. Stevenson, Z. Popovic, C. Hamilton, Z. Zhou, C. Breen, J. Steckel, V. Bulovic, M. Bawendi, S. C. Sullivan, P. T. Kazlas, *Nat. Photonics* **2013**, *7*, 407.
[26] X. Dai, Z. Zhang, Y. Jin, Y. Niu, H. Cao, X. Liang, L. Chen, J. Wang, X. Peng, *Nature* **2014**, *515*, 96.
[27] D. V. Talapin, J.-S. Lee, M. V. Kovalenko, E. V. Shevchenko, *Chem. Rev.* **2010**, *110*, 389.
[28] V. I. Klimov, A. A. Mikhailovsky, D. W. McBranch, C. A. Leatherdale, M. G. Bawendi, *Science* **2000**, *287*, 1011.
[29] A. L. Efros, D. J. Nesbitt, *Nat. Nanotechnol.* **2016**, *11*, 661.
[30] N. Oh, B. H. Kim, S.-Y. Cho, S. Nam, S. P. Rogers, Y. Jiang, J. C. Flanagan, Y. Zhai, J.-H. Kim, J. Lee, Y. Yu, Y. K. Cho, G. Hur, J. Zhang, P. Trefonas, J. A. Rogers, M. Shim, *Science* **2017**, *355*, 616.
[31] Y. Yang, Y. Zheng, W. Cao, A. Titov, J. Hyvonen, J. R. Manders, J. Xue, P. H. Holloway, L. Qian, *Nat. Photonics* **2015**, *9*, 259.
[32] W. K. Bae, Y.-S. Park, J. Lim, D. Lee, L. A. Padilha, H. McDaniel, I. Robel, C. Lee, J. M. Pietryga, V. I. Klimov, *Nat. Commun.* **2013**, *4*, 3661.
[33] X. Gong, Z. Yang, G. Walters, R. Comin, Z. Ning, E. Beauregard, V. Adinolfi, O. Voznyy, E. H. Sargent, *Nat. Photonics* **2016**, *10*, 253.
[34] A. Jane, O. Voznyy, S. Hoogland, M. Korkusinski, P. Hawrylak, E. H. Sargent, *Nano Lett.* **2016**, *16*, 6491.
[35] C. R. Kagan, C. B. Murray, *Nat. Nanotechnol.* **2015**, *10*, 1013.

[36] L. Sun, J. J. Choi, D. Stachnik, A. C. Bartni, B.-R. Hyun, G. G. Malliaras, T. Hanrath, F. W. Wise, *Nat. Nanotechnol.* **2012**, *7*, 369.
[37] W. K. Bae, L. A. Padilha, Y.-S Park, H. McDaniel, I. Robel, J. M. Pietryga, V. I. Klimov, *ACS Nano* **2013**, *7*, 3411.
[38] M. K. Choi, J. Yang, K. Kang, D. C. Kim, C. Choi, C. Park, S. J. Kim, S. I. Chae, T.-H. Kim, J. H. Kim, T. Hyeon, D.-H. Kim, *Nat. Commun.* **2015**, *6*, 7149.
[39] S. Choi, H. Lee, R. Ghaffari, T. Hyeon, D.-H. Kim, *Adv. Mater.* **2016**, *28*, 4203.
[40] S. Lee, A. Reuveny, J. Reeder, S. Lee, H. Jin, Q. Liu, T. Yokota, T. Sekitani, T. Isoyama, Y. Abe, Z. Suo, T. Someya, *Nat. Nanotechnol.* **2010**, *11*, 472.
[41] S.-I. Park, Y. Xiong, R.-H. Kim, P. Elvikis, M. Meitl, D.-H. Kim, J. Wu, J. Yoon, C.-J. Yu, Z. Liu, Y. Huang, K.-C. Hwang, P. Ferreira, X. Li, K. Choquette, J. A. Rogers, *Science* **2009**, *325*, 977.
[42] L. Kim, P. O. Anikeeva, S. A. Coe-Sullivan, J. S. Steckel, M. G. Bawendi, V. Bulović, *Nano Lett.* **2008**, *8*, 4513.
[43] J. Yang, M. K. Choi, D.-H. Kim, T. Hyeon, *Adv. Mater.* **2016**, *28*, 1176.
[44] T. H. Kim, K.-S. Cho, E. K. Lee, S. J. Lee, J. Chae, J. W. Kim, D. H. Kim, J.-Y. Kwon, G. Amaratunga, S. Y. Lee, B. L. Choi, Y. Kuk, J. M. Kim, K. Kim, *Nat. Photonics* **2011**, *5*, 176.
[45] B. H. Kim, M. S. Onses, J. B. Lim, S. Nam, N. Oh, H. Kim, K. J. Yu, J. W. Lee, J.-H. Kim, S.-K. Kang, C. H. Lee, J. Lee, J. H. Shin, N. H. Kim, C. Leal, M. Shim, J. A. Rogers, *Nano Lett.* **2015**, *15*, 969.

ADVANCED MATERIALS

Supporting Information

for *Adv. Mater.*, DOI: 10.1002/adma.201703279

Extremely Vivid, Highly Transparent, and Ultrathin Quantum Dot Light-Emitting Diodes

Moon Kee Choi, Jiwoong Yang, Dong Chan Kim, Zhaohe Dai, Junhee Kim, Hyojin Seung, Vinayak S. Kale, Sae Jin Sung, Chong Rae Park, Nanshu Lu, Taeghwan Hyeon, and Dae-Hyeong Kim**

Supporting Information

Extremely Vivid, Highly Transparent, and Ultrathin Quantum Dot Light-Emitting Diodes

Moon Kee Choi[†], Jiwoong Yang[†], Dong Chan Kim[†], Zhaohe Dai, Junhee Kim, Hyojin Seung, Vinayak S. Kale, Sae Jin Sung, Chong Rae Park, Nanshu Lu, Taeghwan Hyeon, and Dae-Hyeong Kim**

Dr. M. K. Choi, Dr. J. Yang, D. C. Kim, J. Kim, H. Seung, V. S. Kale, Prof. T. Hyeon, and Prof. D.-H. Kim
Center for Nanoparticle Research, Institute for Basic Science (IBS), Seoul 151-742, Republic of Korea
School of Chemical and Biological Engineering and Institute of Chemical Processes, Seoul National University, Seoul 151-742, Republic of Korea
[*]E-mail: dkim98@snu.ac.kr (D.-H.K.) and thyeon@snu.ac.kr (T.H.)
[†]Dr. M. K. Choi, Dr. J. Yang, and D. C. Kim contributed equally to this work

Z. Dai, and Prof. N. Lu
Center for Mechanics of Solids, Structures and Materials, Department of Aerospace Engineering and Engineering Mechanics, Department of Biomedical Engineering, Texas Materials Institute, University of Texas at Austin, Austin, TX 78712, USA

S. J. Sung, Prof. C. R. Park
Research Institute of Advanced Materials, Department of Materials Science and Engineering, Seoul National University, Seoul 08826, Republic of Korea

Supporting Methods

1.1. Synthesis of QDs

Three different types of QDs (red, green, and blue) were synthesized according to the procedures outlined below. Cadmium oxide (CdO, >99.99%), selenium powder (Se, 99.999%), zinc acetate ($Zn(OAc)_2$, 99.99%), S powder (S, 99.99%), oleic acid (OA, 90%), 1-octadecene (1-ODE, 90%), trioctylphosphine (TOP, 90%), tributylphosphine (TBP, 95%), 1-octanethiol (98.5%), cyclohexane (anhydrous, 99.5%), and ethanol (anhydrous, 99.5%) were purchased from Sigma-Aldrich, USA. OA and 1-ODE were degassed at 120 ℃ for 4 h before use. The as-synthesized QDs were treated with OA, TOP, or thiol for ligand-exchange.

1.1.1. Synthesis of red QDs

Red CdSe/CdS/ZnS core/shell/shell QDs were synthesized by reacting metal-oleate complexes with trioctylphosphine selenide (TOPSe, 1 M).[S1, S2] Cation precursor mixtures were prepared by reacting 1.2 mmol of CdO in a mixture of 1.5 mL of OA and 20 mL of 1-ODE under vacuum for 2 h at 120 °C. The mixture was then heated to 300 °C under Ar. At this temperature, TOPSe (1 M) was rapidly injected and the reaction was kept at 300 °C to obtain CdSe cores. 0.9 mmol of 1-octanethiol was then slowly introduced and the reaction was held at 300 °C to form CdS shells. After 40 min, 4.8 mmol of $Zn(oleate)_2$ and 4.8 mmol of tributylphosphine sulfide (TPBS; 2 M) were slowly introduced. The reaction was kept at 300 °C to form ZnS shells. After 20 min, 1.2 mmol $Zn(oleate)_2$ and 1.0 mL 1-octanthiol were swiftly injected into the reaction mixture for further growth of the ZnS shells. The products were purified by precipitation/re-dispersion using cyclohexane and acetone.

1.1.2. Synthesis of green QDs

Green CdSe/ZnS core/shell QDs were synthesized by a reaction between metal-oleate complexes, TOPSe (1 M), and trioctylphosphine sulfide (TOPS, 1 M). Cation precursor mixtures were prepared by reacting 0.2 mmol CdO and 3.5 mmol $Zn(OAc)_2$ in a mixture of 4.0 mL OA and 15 mL 1-ODE under vacuum for 2 h at 120 °C. The mixture was then heated to 300 °C under Ar. At this temperature, 0.2 mmol of TOPSe (2 M) was rapidly injected, followed by the injection of 3.5 mmol of TOPS (2 M) to form ZnS shells. Total reaction time and introduction of shell precursors were adjusted to control shell thickness. The reaction mixture was held at 300 °C for 3 min and 6 min to obtain 6-nm- and 7-nm-sized core/shell green QDs. For the synthesis of 9-nm-sized core/shell green QDs, the total reaction time was increased to 12 min with the introduction of the additional shell precursors (1 mmoL of 1-octanthiol). To obtain QDs with thicker shells (10 nm and 11 nm), 1 mmol of $Zn(oleate)_2$ and 1 mL of 1-octanthiol were slowly introduced into the reaction mixture containing 9-nm-sized QDs. The reaction was further held at 300 °C for 2 min and 8 min for 10-nm- and 11-nm-sized QDs, respectively. The products were purified by precipitation/re-dispersion using cyclohexane and acetone.

1.1.3. Synthesis of blue QDs

Blue CdSe/ZnS core/shell QDs were synthesized by reacting metal-oleate complexes with elemental Se and S. The cation precursor mixtures were prepared by reacting 1.0 mmol of CdO and 9.0 mmol of $Zn(OAc)_2$ in a mixture of 8.0 mL of OA and 15.0 mL of 1-ODE under vacuum for 2 h at 120 °C. The mixture was then heated to 300 °C under Ar. At this temperature, a chalcogenide precursor solution (3.0 mL of 1-ODE containing 1.8 mmol of S and 0.2 mmol of Se) was rapidly injected to obtain blue-emitting QD cores. After 10 min, 8.0 mmol of TBPS solution (2 M) was slowly introduced and the reaction was kept at 310 °C for 50 min to form ZnS shell. 2.5 mmol of $Zn(oleate)_2$ and 1 mL of 1-octanthiol were slowly

injected into the reaction mixture for further growth of the ZnS shell. The products were purified by precipitation/re-dispersion using cyclohexane and acetone.

1.1.4. Synthesis of ZnO nanoparticles

0.48 g of KOH in 25 ml methanol was added dropwise to 1.23 g of $Zn(OAc)_2 \cdot 2H_2O$ in 55 ml methanol over 2 h at 60 °C in ambient conditions. This solution is reacted for 2 h at 60 °C. The product was purified by repeating the precipitation/redispersion method using hexane and isopropyl alcohol mixture and redispersed in butanol. Before used as the electron transport layer, the solution was processed through a 200-nm porous cellulose acetate filter.

1.2. Material characterization

TEM analysis was performed using JEM-ARM200F microscope (JEOL) installed at the National Center for Inter-university Research Facilities (NCIRF) at Seoul National University and JEM-2100F. EDS analysis was performed at the Cd *L*-edge, Se *L*-edge, Zn *K*-edge, and S *K*-edge. AFM data were collected in tapping and conductive AFM modes with a Demension iCON (Bruker) and Multimode 8 (Bruker). The composition of the thin alumina overlayer was characterized using a Sigma probe (Thermo Scientific). Absorption spectra were recorded with a Cary 5000E spectrometer (Agilent). PL spectra were obtained with an FLS980 spectrometer (Edinburgh Instruments). The PL quantum yield was acquired by comparing the PL intensities of the QD solution and those of a reference dye solution (Thermo Scientific) at the same excitation wavelength and the same optical absorbance (0.1). Electrochemical impedance analysis was performed using an AUT302N electrochemical workstation combined with the FRA32M module (Autolab).

1.3. Time-resolved PL lifetime measurements

Time-resolved PL lifetime (TRPL) spectra were measured by a time-correlated single-photon-counting module in a FLS 980 spectrometer (Edinburgh Instruments). QDs in devices and various films (SiO_2/QDs, ITO/HTL/QDs/ZnO/ITO, ITO/HTL/QDs/m-ZnO/ITO) were irradiated using a ~376 nm pulsed laser (EPL-375). The pulse width and repetition rate were ~74.5 ps and 2 MHz, respectively. The emitted photons were spectrally dispersed in a monochromator (1,800 gr mm^{-1}) and collected by a microchannel plate photomultiplier (response width < 25 ps) at the emission maximum of each sample. The measured time window was 200 ns with 8,192 data channels. For applied-voltage dependent TRPL measurements, a source meter (Keysight U8031A) was used to power the Tr-QLEDs. The experiments were conducted under applied voltages less than the turn-on voltages to exclude the effect of EL.

Average carrier lifetimes of the samples were determined based on multi-exponential fits of QD decay ($F(t) = a_1 e^{-t/\tau 1} + a_2 e^{-t/\tau 2} + a_3 e^{-t/\tau 3}$ and $< \tau > = \Sigma (a_i \tau_i^2) / \Sigma (a_i \tau_i)$). Single-exciton radiative lifetimes were obtained from mono-exponential fits from slow components of the QD decay on glass and used for the multi-exponential fitting process.

1.4. Fabrication of Tr-QLEDs

Teflon™ (DuPont) was spin-coated onto cleaned glass substrates and gradually heated. The encapsulation layer (a double-layer structure of parylene-C and epoxy (SU8-2000.5, MicroChem)) was then stacked on the Teflon™ layer. 500-nm-thick parylene-C was conformally coated on the Teflon™ layer and a 600-nm-thick epoxy layer was spin-coated, UV-cured, and annealed on top. The critical temperature of parylene-C is 180 °C, so the following heat treatments were conducted below 180 °C in order to prevent degradation. ITO was sputtered on the encapsulation film (30 W, 30 min, 0.67 Pa, 150 °C) and patterned. After

cleaning the samples with acetone/isopropanol, the surface was treated with O_2 plasma (15 W, 1 min, 13 Pa, 100 sccm). PEDOT:PSS was then spin-coated onto the plasma-treated ITO and annealed at 150 °C for 30 min. In order to minimize the damage caused by humidity and O_2, the sample was then moved to an Ar-filled glove box. TFB in m-xylene (0.5 wt%) was spin-coated and annealed at 150 °C for 30 min. Colloidal QDs in cyclohexane and ZnO nanoparticles in butanol were stacked by spin-coating and annealing at 150 °C in a layer-by-layer manner. A 2-nm-thick Al layer was thermally evaporated and oxidized for 10 min under ambient conditions. Using a shadow mask, a patterned top ITO was sputtered using the same conditions used for the bottom ITO. The top encapsulation double layer (parylene-C and epoxy layer) was deposited to protect the Tr-QLEDs. The encapsulated device could be easily peeled because of the low adhesive force between the Teflon^{TM} and parylene-C layers. After etching the encapsulation layer on the contact region, electrical contacts were established using Ag paste and Cu wires. To obtain stretchable Tr-QLED, Tr-QLED was conformally integrated on 150% pre-stretched elastomer (VHB, 3M) which was gradually shrunk to its original length, forming a wavy structure with numerous crumpling sites.

1.5. Device characterization

The current–voltage curves of Tr-QLEDs were measured with a Keithley 2436 source meter and the brightness was measured with a CS-2000 spectrophotometer. Single-cell measurements of the Tr-QLEDs were performed at room temperature in an Ar-filled glove box without encapsulation, and all ultrathin Tr-QLEDs in Figure 3 were operated in ambient conditions.

1.6. Fabrication of a simple diode structure

To further confirm the protective role of the ETL_{A_x}, a simple diode structure was designed and fabricated using ETL_{A_x}-coated QD films with sputtered top ITO electrode (Figure S6). Without ETL modification, more direct conducting paths are constructed between top and bottom electrode during sputtering process and these conducting paths can cause the short-circuiting or high leakage current under low voltage.

1.7. Measurement of water vapor transmission rate and oxygen transmittance rate

The water vapor transmission rate of the double-layered encapsulation (parylene-C and epoxy, total thickness ~1.2 μm) was measured with PERMATRAN-W® Model 3/33 (MOCON Inc). The exposed area was 25 cm^2 and the measurement was performed under 38 °C, 100% RH. The oxygen transmittance rate was measured with OX-TRAN® 2/21 (MOCON Inc). The exposed area was 50 cm^2 and the measurement was performed under 23 °C, 760.00 mmHg.

Supporting Texts

2.1. Previous progresses and unmet requirements for transparent displays

Figure S1 compares brightness and transmittance of the previously reported transparent LEDs and the current Tr-QLEDs. We compare these two factors, since they are the most important key factors of see-through displays. The representative EL performance and transmittance of transparent LEDs are also summarized in Table S1. Considerable efforts have been devoted to develop transparent LEDs mostly based on organic and/or polymer emitting materials. However, their EL performance is poor in comparison with the performance of their non-transparent counterparts, largely because of constraints in the electrode material selection and damages in active layers during the deposition process of transparent electrodes. For instance, ordinary transparent conducting oxides (TCOs), such as indium tin oxide (ITO), may not be preferred for organic LEDs as a top electrode (solid dots in Figure S1), because their harsh deposition processes, such as sputtering, damage vulnerable organic light emissive layers. Thick inorganic ETLs have been employed to protect light emissive layers, but the resulting transparent LEDs exhibit relatively low luminance and high turn-on voltages because of charge imbalances and high internal resistances within the device. Thin metal films or metal grids (shaded dots in Figure S1) have been applied as alternatives, but they present semi-transparency and non-uniform conduction characteristics caused by small apertures and grid geometries. Transparent displays with nanomaterial-based electrodes (*i.e.*, graphene, carbon nanotubes, and metal nanowires; hollow dots in Figure S1) have also been explored, but their EL characteristics and transparencies are not satisfactory yet. Therefore, a novel device structure and breakthroughs in electrode and carrier transport materials are required toward the high performance next generation transparent display.

2.2. The effect of the ETL_{A_x} on the charge kinetics of Tr-QLEDs

To study the effect of the ETL_{A_x} on the charge kinetics of the Tr-QLEDs, we conducted electrochemical impedance measurement. Figure S11a shows the Cole-Cole plots for Tr-QLEDs with various alumina overlayer thicknesses. We employed the equivalent circuit model for data analysis (inset of Figure 2f). The C_P and R_{ct} of the Tr-QLEDs with the various ETL_{A_x} are plotted depending on the applied voltage (Figure S11b; raw data in Figure S11c and d).

Under the low applied bias ($V_{app} < V_{turn\text{-}on}$), the C_P values are similar for all ETL_{A_x} devices. The capacitance is similar to their geometrical capacitance, $C_0 = \varepsilon\varepsilon_0 A\ d$.[S3] R_{ct} becomes larger with increasing the overlayer thickness because of insulating properties of alumina.

Under the high forward bias ($V > V_{turn\text{-}on}$), the different tendencies of the C_P and R_{ct} change depending on the ETL_{A_x} are shown. The Tr-QLEDs with the alumina overlayers show low C_P value under the applied voltage for device operation (*e.g.*, V = 6 V), while Tr-QLEDs without the alumina overlayer (ETL_{A_0}) exhibit high C_P that is similar to the case with the applied bias under $V_{turn\text{-}on}$. This supports that the ETL_{A_x} is helpful for suppression of the charging effect in the devices under the device operating condition ($V > V_{turn\text{-}on}$) by preventing the excess electron injection.

Moreover, charge kinetics is also optimized with the ETL_{A_x}, in spite of insulating characteristics of the alumina overlayer. In the voltage range of device operation ($V > V_{turn\text{-}on}$), R_{ct} values are significantly reduced for all the devices as the applied voltage increases.[S4] In particular, the reduction in R_{ct} with the overlayers is faster than that without the overlayers (ETL_{A_0}). As a results, the R_{ct} with the optimized overlayer (ETL_{A_2}) is reduced to the

minimum at high applied voltage (> 5 V), indicating the optimized charge transport kinetics (inset of Figure S11d).

2.3. The effect of the shell thickness for improving QD stability

To examine the effect of the shell thickness on the stability of QDs, we irradiated 365 nm UV to the QD films on 120 °C hotplate under the ambient condition (Figure S13e). This photothermal treatment accelerated the decomposition of QD films. The PL decay of 6-nm-thick QDs are dramatically decreased within 10 minutes while that of 10-nm-thick and 11-nm-thick QDs showed stable characteristics even after 20 minutes photothermal treatment. This improved QD stability is due to passivation of defect sites on the surface of the core.

2.4. Optimizing ligands of QDs for high performance Tr-QLEDs

In this study, as-synthesized QDs are passivated with diverse ligands including octylthiol, OA, and TOP. For optimization of the ligands of QDs, post-ligand exchange treatment was conducted. Generally, short-chain ligands are preferred for nanocrystal-based devices because of efficient carrier transport.[14, 27] However, different results are found in our study. Tr-QLEDs using long-chain OA-capped QDs exhibit higher luminance and efficiency than devices employing short-chain capped (*e.g.*, TOP) or as-synthesized QDs (Figure S14b). This highlights that balanced hole/electron injection and controlled carrier recombination are more important than simply enhancing the carrier injection rate.

2.5. Mechanical simulation for deformable Tr-QLEDs

The strain in the brittle ITO electrodes after the pre-stretching and releasing process is important to the mechanical integrity and functional performance (*i.e.*, stretchability and durability) of our devices. For this purpose, we calculate the wavy-structure-induced strain in

our film-like Tr-QLEDs following well-studied analytical solutions about buckled thin films on compliant supports, which considered the incompressibility of the soft VHB substrate.[S5] The multilayer QLED rigid films mainly feature encapsulated 1800 nm-thick parylene-C (modulus: ~4 GPa) and 600-nm-thick epoxy layer (modulus: ~2.8 GPa). The moduli of other layers are within 2 orders of the GPa range, *e.g.* 200 nm-thick ITO (~116 GPa), 50 nm-thick QD (3-5 GPa) and 20 nm-thick PEDOT:PSS (1 GPa) *etc.* Since the VHB substrate has a modulus of 450 kPa (according to 3M datasheets), we can model the ultrathin Tr-QLEDs as a uniform, thin, elastic film. Considering a thin film of thickness h and elastic modulus E_f transferred on a linear elastic substrate of modulus E_s subjected to a pre-stretched strain of ε_{pre}, releasing the prestrain leads to sinusoidal wrinkles with wavelengths and half peak-to-peak amplitude to be

$$\lambda_0 = 2\pi h\left(\frac{\overline{E_f}}{3\overline{E_s}}\right)^{\frac{1}{3}} \text{ and } A_0 = h\sqrt{\frac{\varepsilon_{pre}}{\varepsilon_c}-1} \quad \text{(S1)}$$

respectively, where $\bar{E} = \frac{E}{1-\nu^2}$ is the plane-strain modulus, ν is the Poisson ratio, and $\varepsilon_c = \frac{1}{4}\left(\frac{3\overline{E_s}}{\overline{E_f}}\right)^{\frac{2}{3}}$. When the substrate is an incompressible neo-Hookean material (*e.g.*, VHB used in our device), the wavelength and amplitude become

$$\lambda = \frac{\lambda_0}{(1+\varepsilon_{pre})(1+\xi)^{\frac{1}{3}}} \text{ and } A = \frac{A_0}{\sqrt{1+\varepsilon_{pre}}(1+\xi)^{\frac{1}{3}}} \quad \text{(S2)}$$

where $\xi = \frac{5\varepsilon_{pre}(1+\varepsilon_{pre})}{32}$ results from the geometrical nonlinearity and nonlinear constitutive model.[S5] Consequently, the maximum strain in the thin film is given by $\varepsilon = \frac{2\sqrt{\varepsilon_{pre}\varepsilon_c}(1+\xi)^{\frac{1}{3}}}{\sqrt{1+\varepsilon_{pre}}}$. The maximum strain of the film can represent the strain in ITO because ITO is the top and bottom most layers for the Tr-QLED (Figure 1g). Both SEM observation and 1D height profile measurement of ultrathin Tr-QLED with 50% pre-strain indicate that the wrinkles

exhibit a wavelength of 360 μm and irregular amplitudes (Figure S16). The scattering amplitudes might be attributed to the patterned layers as well as the finite size of the Tr-QLED. Based on the wavelength measurements of ultrathin Tr-QLED with 33% and 50% pre-strain and following above analysis (Figure 3f), we can derive a plane-strain modulus ratio of ~110,000 between the device film and the VHB substrate, which is within the same order of the plane-strain modulus ratio between ITO and VHB. Applying this effective modulus of the film, the analytical solution predicts an amplitude of ~101 μm for devices with 50 % pre-strain, which is in good agreement with experimentally measured amplitude as shown in Figure S16a.

To study the stretchability of the as-fabricated wrinkled Tr-QLED, we should investigate the strain in ITO when the device is subjected to an applied tensile strain ε_{app}. The wavelength and amplitude of a wrinkled film under tensile strain have been solved as

$$\lambda = \frac{1+\varepsilon_{app}}{(1+\varepsilon_{pre})(1+\varepsilon_{app}+\zeta)^{\frac{1}{3}}} \quad \text{and} \quad A = h\frac{\sqrt{\frac{\varepsilon_{pre}-\varepsilon_{app}}{\varepsilon_c}-1}}{\sqrt{1+\varepsilon_{pre}}(1+\varepsilon_{app}+\zeta)^{\frac{1}{3}}} \tag{S3}$$

where $\zeta = \frac{5(\varepsilon_{pre}-\varepsilon_{app})(1+\varepsilon_{pre})}{32}$. The amplitude A vanishes when the applied strain reaches the pre-strain minus the critical strain ε_c. The peak strain in the film is given by[S5]

$$\varepsilon = \frac{2\sqrt{(\varepsilon_{pre}-\varepsilon_{app})\varepsilon_c}(1+\varepsilon_{app}+\zeta)^{\frac{1}{3}}}{\sqrt{1+\varepsilon_{pre}}} \tag{S4}$$

which decays to zero as the applied strain equals to the pre-strain. The wavelength of the wrinkle vs. the applied strain is plotted as the black curve in Figure 3f, which finds good match with experimentally measured wavelengths at three different applied strains. As expected, the wavelength increases with increased applied strain because stretching the wrinkled Tr-QLED is a process of releasing the wrinkles. The blue curve in Figure 3f plots the predicted maximum strain in ITO vs. applied strains. As expected, the peak strain

decreases all the way to zero when $\varepsilon_{app} = \varepsilon_{pre}$, which is 50% for this sample. During the stretching process, the strain in ITO is always below the fracture strain of ITO, which guarantees the stretchability of our Tr-QLED.

Supporting Table

Table S1. Comparison of key characteristics and performances of transparent LEDs.

LED Type	Electrode material		Transparency @ 550 nm	Current efficiency (cd A^{-1}) *	Max. Luminance (cd m^{-2})			Ref.
	Anode	Cathode			Bottom	Top	Total	
OLED	ITO	Au 10 nm	55%	2.5	10,500 (10 V)	-	-	S6
OLED	AZO	ITO	66%	-	-	700 (20 V)	-	S7
OLED	ITO	ITO	75%	38	10,000 (6.5 V)	-	-	10
OLED	ITO	Ag 15 nm	80%	2.3	18,000 (6.7 V)	4,000 (6.7 V)	22,000 (6.7 V)	S8
OLED	ZnS/Ag	ZnS/Cs_2CO_3/Ag	74%	1.6	1,000 (6 V)	900 (6 V)	1,900 (6 V)	S9
OLED	ITO	Graphene	75%	3.1	480 (13 V)	570 (13 V)	1,050 (13 V)	S10
OLED	ITO	laminated ITO	72%	23.1	20,000 (15 V)	20,000 (15 V)	40,000 (15 V)	S11
OLED	Ag 10 nm-MoO_3 2.5 nm	Al 1.5 nm/Ag 15 nm/NPB 50 nm	75%	17.3 lm/W	3,207 (7 V)	3,114 (7 V)	6,321 (7 V)	S12
PLED	Ag NW-PUA	Ag NW-PUA	-	5.6	2,200 (20 V)	-	-	11
PLED	ITO	Au 15 nm	55%	-	210 (60 V)	-	-	S13
PLED	Ag NW-GO	Ag NW-GO	-	4	1,100 (20 V)	1,100 (20 V)	2,200 (20 V)	S14
QLED	Graphene	Graphene	75%	0.45	358 (29 V)	-	-	S15
QLED	ITO	Ag NW	-	5.6	25,040 (7 V)	23,440 (7 V)	48,480 (7 V)	2
QLED	ITO	IZO	72%	0.45	200 (16 V)	-	-	8
QLED	ITO	ITO	70%	3.5	9,146 (15V)	-	-	9
QLED	ITO	ITO	90%	17.52	43,000 (9 V)	30,000 (9 V)	73,000 (9 V)	Ours

* Current efficiency of each device is based on the maximum value by one-side luminance.

Supporting Figures

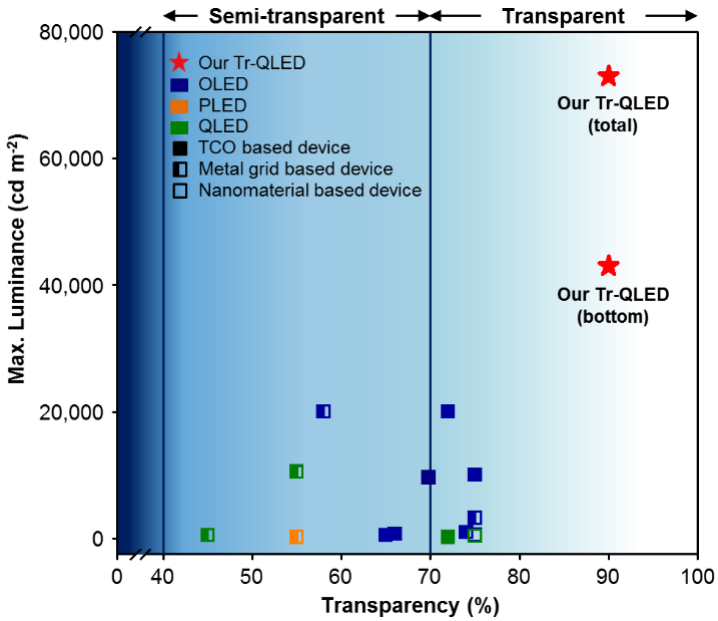

Figure S1. Comparison of key characteristics (luminance and transparency) of transparent LEDs. Transparency at the 550 nm wavelength and maximum EL brightness of various transparent LEDs from previous reports including our Tr-QLEDs are plotted together for comparison. The luminance of each device is plotted based on the maximum luminance by one-side emission.

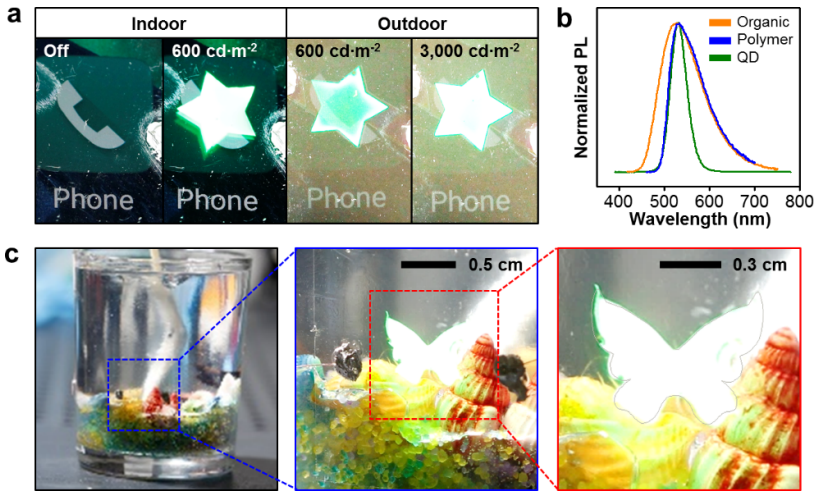

Figure S2. Extremely vivid, highly transparent, and ultrathin quantum dot LEDs. a) Visibility change under ambient light. b) Comparison of the PL spectra of our QD emitter with the typical organic ($Al(C_9H_6NO)_3$; Alq3) and polymer (F8BT) emitter. c) Ultrathin Tr-QLEDs (butterfly pattern) laminated on curved glassware.

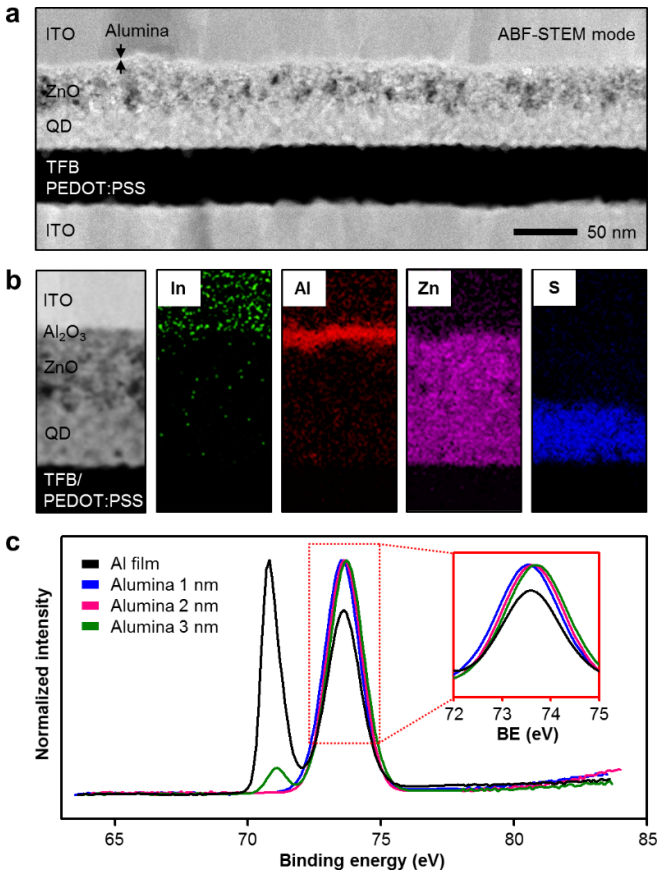

Figure S3. Material characterization of Tr-QLEDs and the alumina overlayers. a) Annular bright field scanning TEM image of Tr-QLEDs. b) Cross-sectional TEM image (left) and corresponding EDS data (right) of Tr-QLEDs. The EDS scan analysis shows the elemental distribution of In (green), Al (red), Zn (purple), and S (blue). c) XPS spectra of the ultrathin alumina overlayers, which confirm the fully oxidized alumina overlayers.

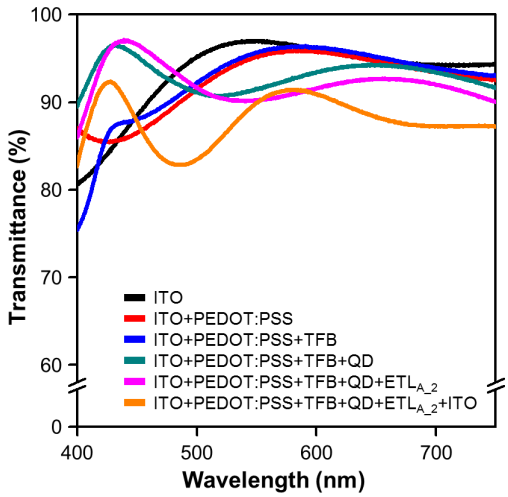

Figure S4. Change in transmittance as stacking the composing layers of the Tr-QLED.

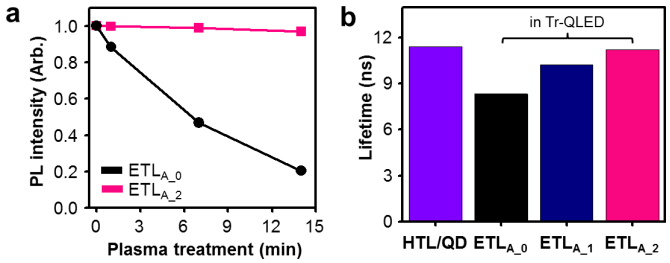

Figure S5. Stability of QDs depending on the ETL structure. a) Relative PL intensities of the QD film with the ETL_{A_0} (black) and ETL_{A_2} (pink) according to the plasma treatment time (Ar, 30 W, 13 Pa). b) Average carrier lifetime of QDs in Tr-QLEDs with ETL_{A_x}.

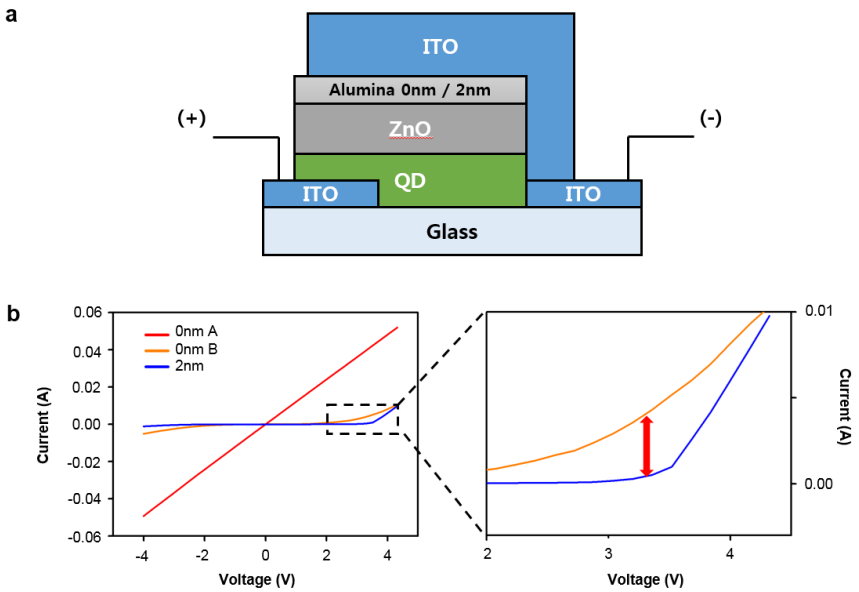

Figure S6. The effect of ETL modification on the operation of diode consisting of ETL_{A_x}-coated QD films and sputtered top ITO electrode. a) the schematic illustration of the diode. b) *I-V* characteristics of diodes with and without alumina overlayers. Without alumina overlayers, some diodes are short-circuited (red line) or show higher leakage current (orange line) than diodes with alumina overlayers (blue line).

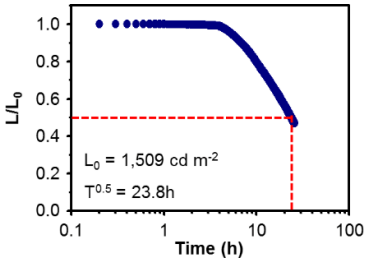

Figure S7. Lifetime of Tr-QLEDs with ETL_{A_2}.

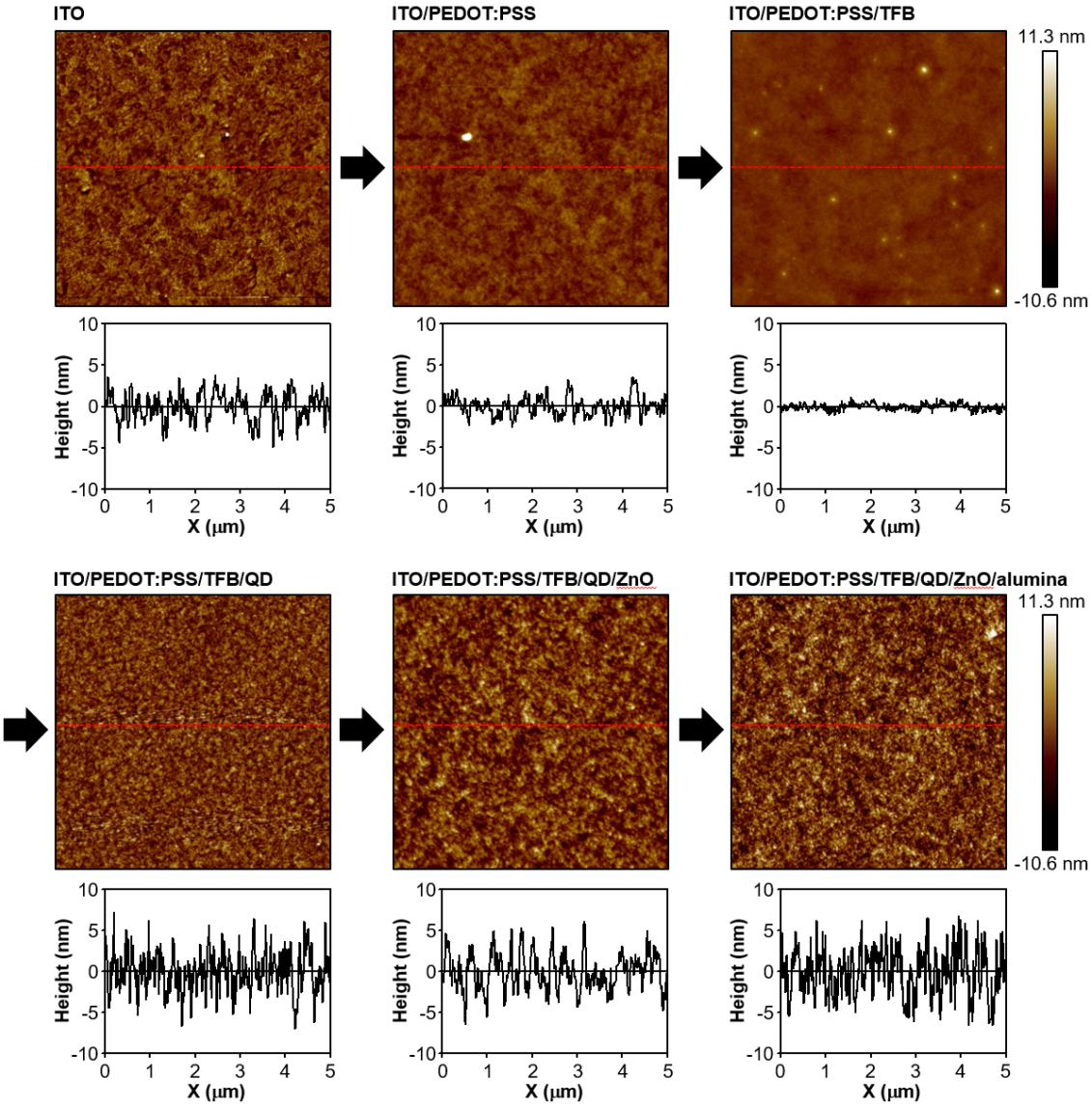

Figure S8. Surface morphology of each layer composing the Tr-QLED which is characterized by AFM. The AFM height image (contact mode; top) and its line-scan profile (bottom) are presented for each layer (ITO, ITO/PEDOT:PSS, ITO/PEDOT:PSS/TFB, ITO/PEDOT:PSS/TFB/QD, ITO/PEDOT:PSS/TFB/QD/ZnO, and ITO/PEDOT:PSS/TFB/QD/ZnO/alumina).

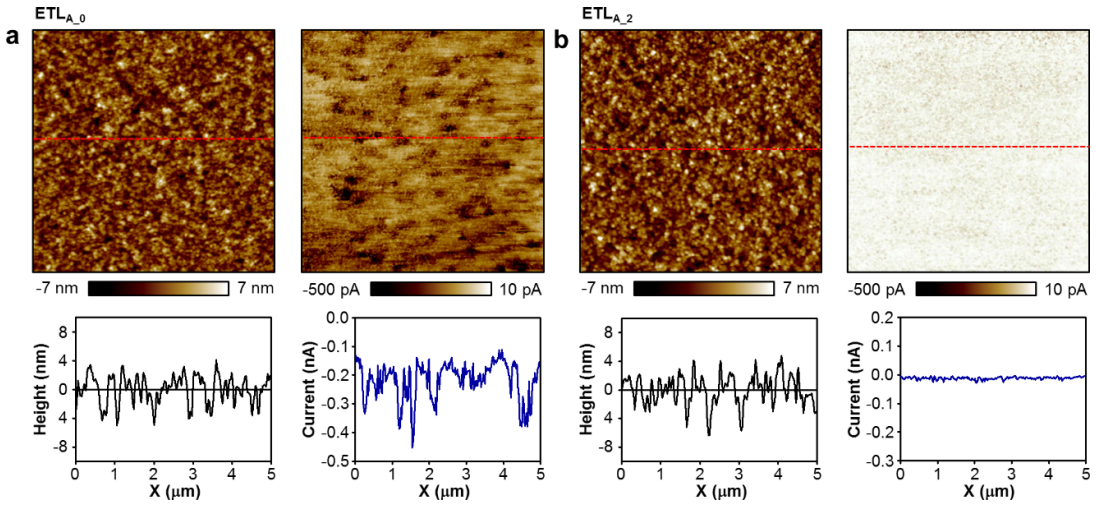

Figure S9. Current distribution of the ITO/HTL/QDs/ETL structure characterized by conductive AFM. a, b) Conductive AFM characterization of the ITO/HTL/QDs/ETL structure without (a; ETL_{A_0}) and with (b; ETL_{A_2}) the alumina overlayer. The surface morphology data (top left), current mapping data (top right), line-scan height profile (bottom left), and line-scan current profile (bottom right) are shown for each device. The amount of current fluctuation in the device with the overlayer is two orders of magnitude less than that of the device without the overlayer, while height profiles (morphology) of each device are similar each other.

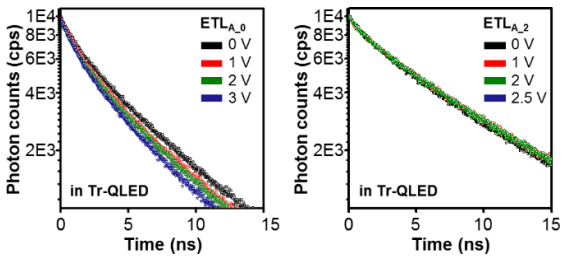

Figure S10. Effect of the ETL_{A_x} on the exciton carrier lifetime of QDs in Tr-QLEDs. TRPL spectra of QDs in Tr-QLEDs under various applied voltages without (left) and with (right) 2 nm-thick alumina overlayer on the ZnO nanoparticle assembly.

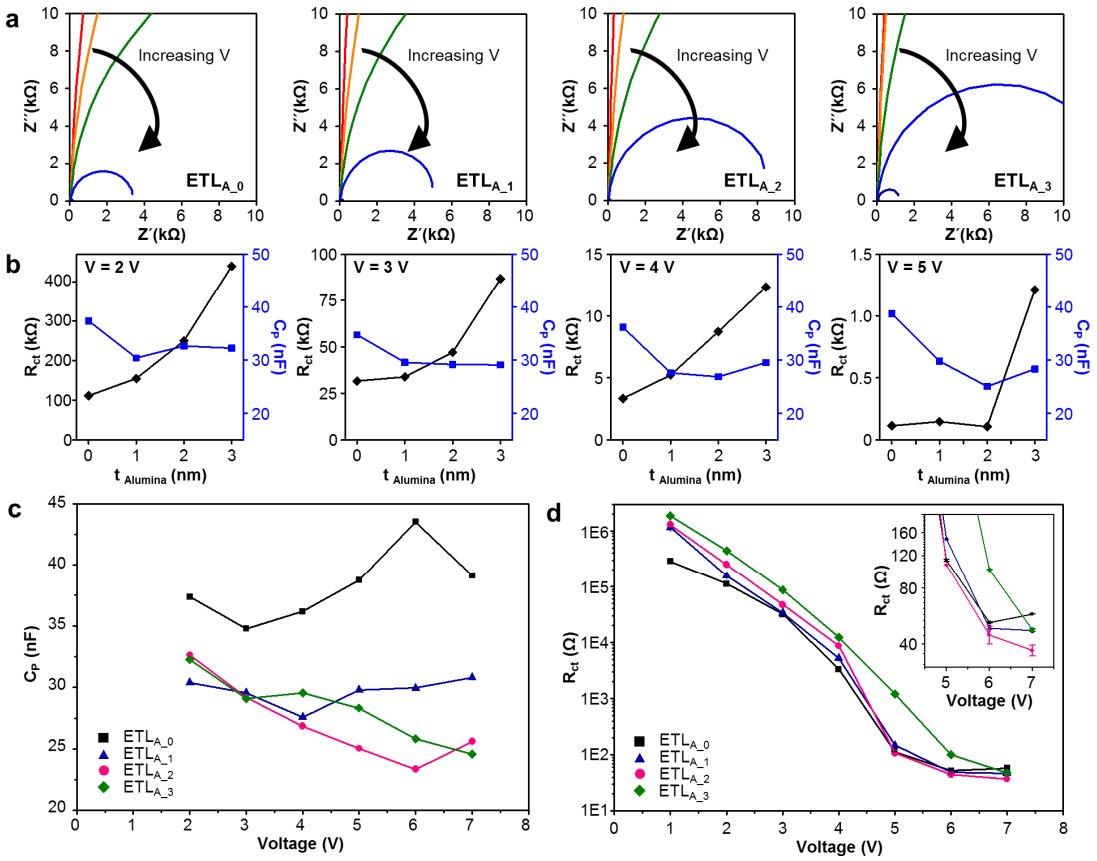

Figure S11. The effect of the ETL_{A_x} on the charge kinetics of Tr-QLEDs. a) Cole-Cole plots of Tr-QLEDs with various ETL_{A_x} under increasing applied voltages. b) Changes in R_{ct} (left axis) and C_P (right axis) of the Tr-QLEDs against the alumina thickness. Applied voltages are varied between 2 V and 7 V from left to right. c, d) Change in C_P (c) and R_{ct} (d) of Tr-QLEDs against the applied voltage. Inset of (d) shows the magnified R_{ct} trend at high operating voltages.

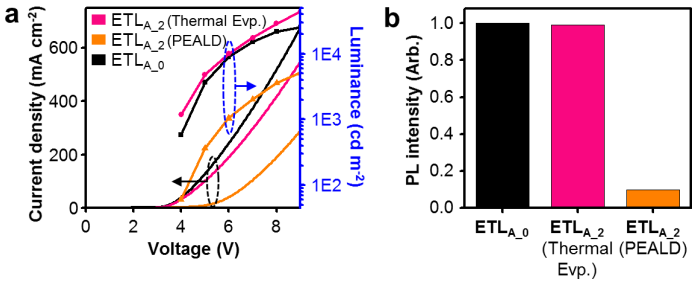

Figure S12. Comparison of Tr-QLEDs with the alumina overlayer oxidized from thermally evaporated aluminum and deposited by PEALD. a, b) *J-V-L* characteristics (a) and relative PL intensity of QDs (b) in Tr-QLEDs.

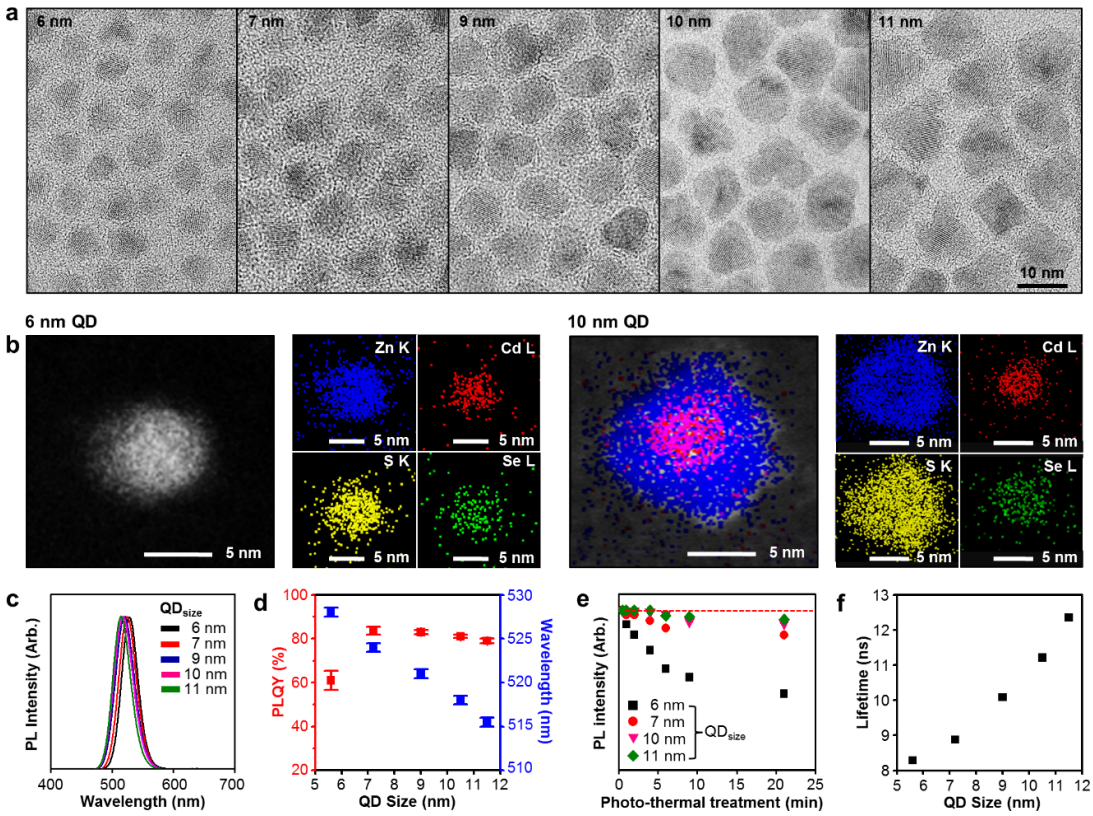

Figure S13. Characterization of QDs with controlled shell thicknesses. a) TEM images of QDs with various shell thicknesses (6 nm, 7 nm, 9 nm, 10 nm, and 11 nm of the total size). b) Scanning TEM image (left) and EDS scan data (right) of 6-nm-thick and 10-nm-thick QDs. EDS mapping images show elemental distributions of Zn (blue), Cd (red), S (yellow), and Se (green). c) PL spectra acquired from the solution containing QDs with various shell thicknesses. d) PL quantum yield (QY) and peak emission wavelength of the QDs. e) Relative PL intensities of various QDs according to the photo-thermal treatment time (250 ^{o}C under UV exposure (16 W at 365 nm) and atmospheric condition). f) Average carrier lifetime of the QDs in Tr-QLEDs.

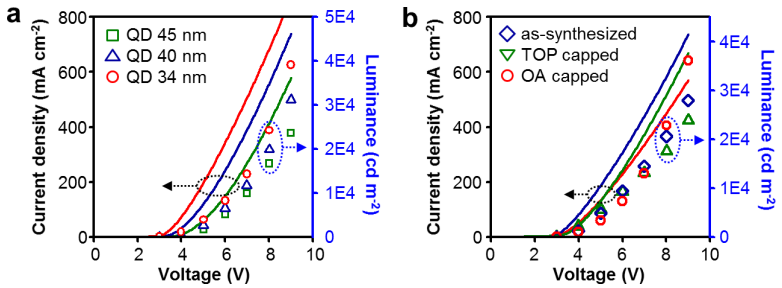

Figure S14. a) *J-V-L* characteristics of Tr-QLED against the thickness of QD layer. Thickness of QD film varied from 34 nm to 45 nm. b) *J–V–L* characteristics of Tr-QLEDs employing QDs with different passivating ligands. The as-synthesized QDs are passivated with diverse ligands (e.g., thiol, OA, and TOP). TOP capped- and OA capped-QDs are prepared by the post-ligand-exchange process.

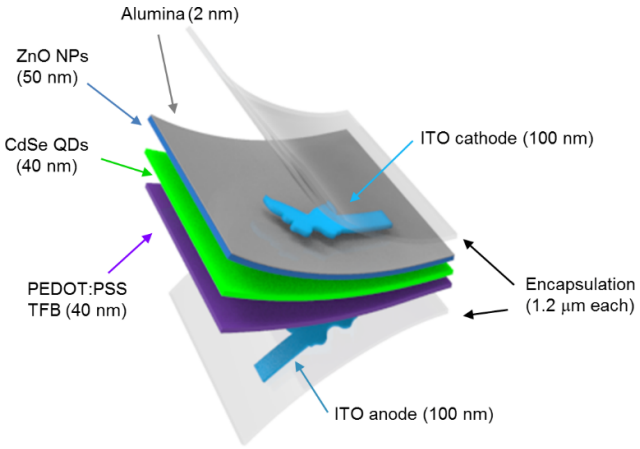

Figure S15. Schematic illustration of the ultrathin and deformable Tr-QLEDs.

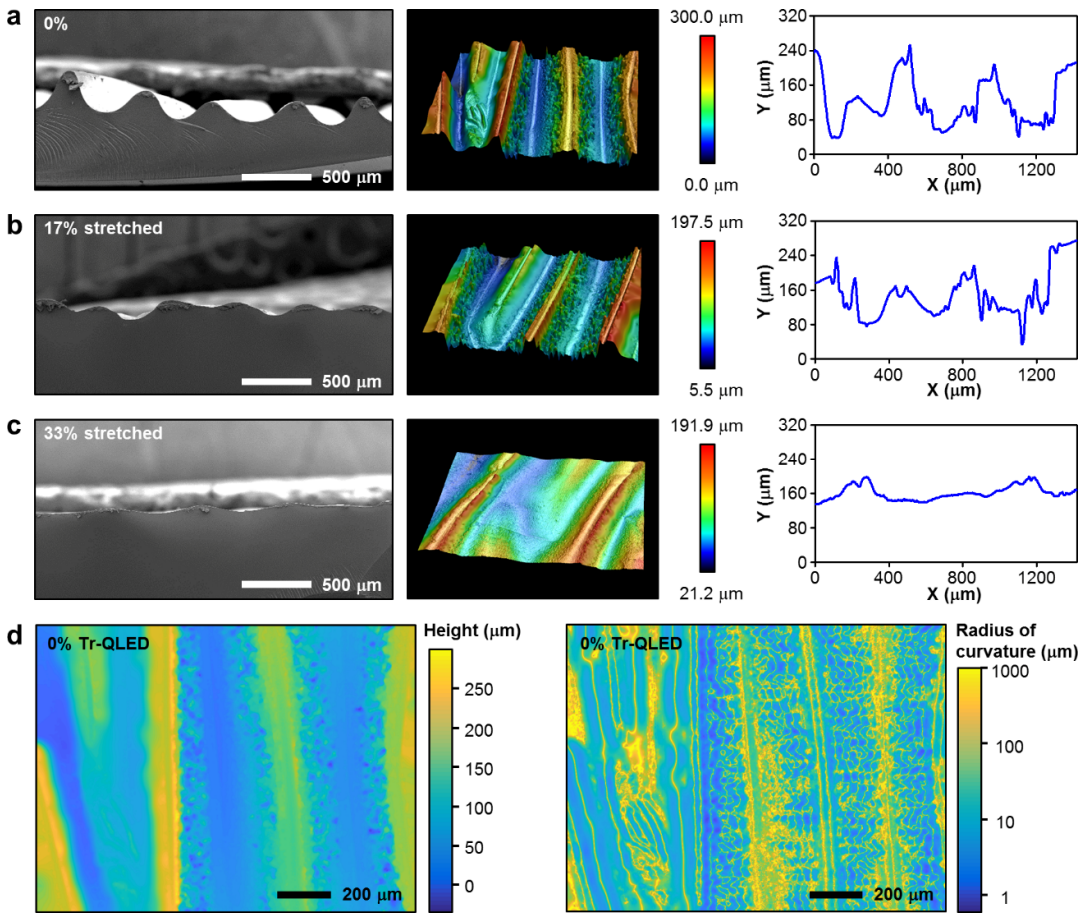

Figure S16. Characterization of stretchable Tr-QLEDs. a-c) Deformable Tr-QLEDs under the applied tensile strain of 0% (a), 17% (b), and 33% (c). The images from left to right show cross-sectional SEM image (left), 3D optical profile (middle), and 1D height profile (right) measured using the PUA replica of wavy Tr-QLEDs. d) The height profile (left) and 2D radius of curvature image (right) of wavy Tr-QLEDs.